Article

Full Stokes imaging polarimetry using dielectric metasurfaces

Ehsan Arbabi, Seyedeh Mahsa Kamali, Amir Arbabi, and Andrei Faraon

ACS Photonics, **Just Accepted Manuscript** • DOI: 10.1021/acsphotonics.8b00362 • Publication Date (Web): 16 Jul 2018

Full Stokes imaging polarimetry using dielectric metasurfaces

Ehsan Arbabi,[†] Seyedeh Mahsa Kamali,[†] Amir Arbabi,[‡] and Andrei Faraon[*,†]

†*T. J. Watson Laboratory of Applied Physics, California Institute of Technology, 1200 E. California Blvd., Pasadena, CA 91125, USA*

‡*Department of Electrical and Computer Engineering, University of Massachusetts Amherst, 151 Holdsworth Way, Amherst, MA 01003, USA*

Abstract

Polarization is a degree of freedom of light carrying important information that is usually absent in intensity and spectral content. Imaging polarimetry is the process of determining the polarization state of light, either partially or fully, over an extended scene. It has found several applications in various fields, from remote sensing to biology. Among different devices for imaging polarimetry, division of focal plane polarization cameras (DoFP-PCs) are more compact, less complicated, and less expensive. In general, DoFP-PCs are based on an array of polarization filters in the focal plane. Here we demonstrate a new principle and design for DoFP-PCs based on dielectric metasurfaces with the ability to control polarization and phase. Instead of polarization filtering, the method is based on splitting and focusing light in three different polarization bases. Therefore, it enables full-Stokes characterization of the state of polarization, and overcomes the 50% theoretical efficiency limit of the polarization-filter-based DoFP-PCs.

Keywords. Dielectric metasurface, nanophotonics, polarization and phase control, division of focal plane, polarization camera.

Polarimetric imaging is the measurement of the polarization state of light over a scene of interest. While spectral and hyperspectral imaging techniques provide information about the molecular and material composition of a scene,[1,2] polarimetric imaging contains information about the shape and texture of reflecting surfaces, the orientation of light emitters, or the optical activity of various materials.[3,4] This additional information has led to many applications for imaging polarimetry ranging from astronomy and remote sensing to marine biology and medicine.[3,5–11] Therefore, several methods have been developed over the past decades to enable mapping of the polarization state over an extended scene.[11–18]

Generally, polarimetric imaging techniques can be categorized into three groups: division of amplitude, division of aperture, and division of focal plane.[3] All of these techniques are based on measuring the intensity in different polarization bases and using them to estimate the full Stokes vector or a part of it. DoFP-PCs are less expensive, more compact, and require less complicated optics compared to the two other categories of polarimetric imaging systems.[3,16–18] In addition, they require much less effort for registering images of different polarizations as the registration is automatically achieved in the fabrication of the polarization sensitive image sensors. The advances in micro/nano-fabrication have increased the quality of DoFP-PCs and reduced their fabrication costs, making them commercially available. DoFP-PCs either use a birefringent crystal to split polarizations,[19,20] or thin-film[17,21] or wire-grid[11,16,22] polarization filters. To enable the measurement of degree of circular polarization, form-birefringent quarter waveplates were integrated with linear polarizers in the mid-IR.[23] Recently, liquid crystal retarders have been integrated with linear polarization filters to enable full Stokes polarimetric imaging by implementing circular[24] and elliptical polarization filters.[25,26] An issue with the previously demonstrated DoFP-PCs is that they all have a theoretical efficiency limit of 50% because they use polarization filters,[3] or spatially block half of the aperture.[20]

Optical metasurfaces are a category of nano-fabricated diffractive optical elements comprised

of nano-scatterers on a surface[27–45] that are judiciously designed to control optical wavefronts. They have enabled high-efficiency phase and polarization control with large gradients.[31,32,37,38,42,46] In addition, their compatibility with conventional microfabrication techniques allows for their integration into optical metasystems.[47–50]

Metasurfaces have previously been used for polarimetry,[51–59] but not polarimetric imaging. An important capability of high contrast dielectric metasurfaces is the simultaneous control of polarization and phase.[46] Here, we use this capability to demonstrate a dielectric metasurface mask for DoFP-PCs with the ability to fully measure the Stokes parameters, including the degree of circular polarization and helicity. Since the mask operates based on polarization splitting and focusing instead of polarization filtering, it overcomes both the 50% theoretical efficiency limit, and the one-pixel registration error (resulting from distinct physical areas of the polarization filters) of the previously demonstrated DoFP-PCs.[3] In addition, unlike the previously demonstrated full Stokes DoFP-PCs, the metasurface is fabricated in a single dielectric layer and does not require integration of multiple layers operating as retarders and polarization filters. The mask is designed for 850-nm center wavelength. The polarization cross-talk ranges from 10% to 15% for pixel sizes from 7.2 μm to 2.4 μm when using an 850-nm LED as the light source. In addition, to demonstrate that the metasurface DoFP-PC can be used to form polarization images over extended scenes we imaged a custom polarization mask that we fabricated. To the best of our knowledge, this is the first demonstration of a DoFP-PC mask that measures the polarization state completely and is not based on polarization filtering.

There are several representations for polarization of light.[60] Among them, the Stokes vector formalism has some conceptual and experimental advantages since it can be used to represent light with various degrees of polarization and can be directly determined by measuring the power in certain polarization bases.[60] Therefore, most imaging polarimetry systems determine the Stokes vector $\mathbf{S} = [S_0, S_1, S_2, S_3]$,[3] where the components are defined as $S_0 = I$, $S_1 = I_{\mathrm{x}} - I_{\mathrm{y}}$, $S_2 = I_{45} - I_{-45}$, and $S_3 = I_{\mathrm{R}} - I_{\mathrm{L}}$. Here I is the total intensity, I_{x}, I_{y}, I_{45}, and I_{-45} are the intensity of light in linear polarization bases along the x, y, +45-degree, and -45-degree directions,

respectively. I_{R} and I_{L} denote the intensities of the right-hand and left-hand circularly polarized light. Usually, S_1, S_2, and S_3 are normalized to S_0 such that their value changes between -1 and +1. To fully characterize the state of polarization, all these intensities should be determined. A conventional setup used to measure the full Stokes vector is shown in **Figure 1**a: a waveplate (half or quarter), followed by a Wollaston prism and a lens that focuses the beams on photodetectors. One can determine the four Stokes parameters[60] from the detector signals acquired under three different conditions: without a waveplate, with a half-waveplate (HWP) inserted, and with a quarter-waveplate (QWP) inserted in the setup. An optical metasurface with the ability to fully control phase and polarization of light[46] can perform the same task over a much smaller volume and without changing any optical components. The metasurface can split any two orthogonal states of polarization and simultaneously focus them to different points with high efficiency and on a micron-scale. This is schematically shown in **Figure 1**a. Such a metasurface can be directly integrated on an image sensor for making a polarization camera. To fully measure the Stokes parameters, the projection of the input light on three different polarization basis sets should be measured. A typical choice of basis is horizontal/vertical (H/V), $\pm 45^{\circ}$ linear, and right-hand-circular/left-hand-circular (RHCP/LHCP) that can be used to directly measure the Stokes parameters. **Figure 1**b shows a possible configuration where the three metasurface polarization beam-splitters (PBS) are multiplexed to make a superpixel, comprising of six pixels on the image sensor. Each image sensor pixel can then be used to measure the power in a single polarization state. A schematic illustration of a superpixel is shown in **Figure 1**c. The colors are only used to distinguish different parts of the super pixel more easily, and do not correspond to actual wavelengths. The blue nano-posts separate and focus RHCP/LHCP, the green ones separate $\pm 45^{\circ}$, and the red ones separate H/V.

The metasurface platform we use here is based on dielectric birefringent nano-post structures.[46] As seen in **Figure 2**a, the metasurface is composed of α-Si nano-posts with rectangular cross-sections on a low-index fused silica substrate. With a proper choice of the α-Si layer thickness and lattice constant (650 nm and 480 nm respectively for an operating wavelength of 850nm), the

nano-posts can provide full and independent 2π phase control over x and y-polarized light where x and y are aligned with the axes of the nano-post (see Supporting Information Fig. S1).[61] Using the phase versus dimension graphs, one can calculate the nano-post dimensions required to provide a specific pair of phase values, ϕ_{x} and ϕ_{y}, as shown in **Figure 2**b. This allows for designing a metasurface that controls x and y-polarized light independently. With a simple generalization, the same can be applied to any two orthogonal linear polarizations using nano-posts that are rotated around their optical axis with the correct angle to match the new linear polarizations (e.g., the x′-y′ axis in **Figure 2**c). An important and interesting point demonstrated in[46] is that this can be done on a point-by-point manner, where the polarization basis is different for each nano-post. This property allows us to easily design the metasurface PBS for the two linear bases of interest. Moreover, as demonstrated in,[46] an even more interesting property of this seemingly simple structure is that the independent control of orthogonal polarizations can be generalized to elliptical and circular polarizations as well (with the small drawback that the output and input polarizations should have opposite handedness). To make the design process clear, here we reiterate the results presented in the supplementary material of.[46]

The operation of a nano-post can be modeled by a Jones matrix relating the input and output electric fields (i.e., $\mathbf{E}^{\mathrm{out}} = \mathbf{T}\mathbf{E}^{\mathrm{in}}$). For the rotated nano-post shown in **Figure 2**c, the Jones matrix can be written as:

$$\mathbf{T} = \begin{bmatrix} T_{xx} & T_{xy} \\ T_{yx} & T_{yy} \end{bmatrix} = \mathbf{R}(\theta) \begin{bmatrix} \mathrm{e}^{i\phi_{x'}} & 0 \\ 0 & \mathrm{e}^{i\phi_{y'}} \end{bmatrix} \mathbf{R}(-\theta), \tag{1}$$

where $\mathbf{R}(\theta)$ denotes the rotation matrix by an angle θ in the counter-clockwise direction. Here we have assumed unity transmission since the nano-posts are highly transmissive. We note here that the right hand side of Equation 1 is a unitary and symmetric matrix. Using only these two conditions (i.e., unitarity and symmetry), we find $T_{xy} = T_{yx}$, $|T_{yx}| = \sqrt{1 - |T_{xx}|^2}$, and $T_{yy} = -\exp(\mathrm{i}2\angle T_{yx})T_{xx}$. As one would expect, these equation restrict the available number of controllable parameters to three ($|T_{xx}|$, $\angle T_{xx}$, $\angle T_{yx}$), corresponding to the three available physical parameters ($\phi_{x'}$, $\phi_{y'}$, and θ). Using these relations to simplify $\mathbf{E}^{\mathrm{out}} = \mathbf{T}\mathbf{E}^{\mathrm{in}}$, we can rewrite it to

find the Jones matrix elements in terms of the input and output fields:

$$\begin{bmatrix} E_x^{\text{out}*} & E_y^{\text{out}*} \\ E_x^{\text{in}} & E_y^{\text{in}} \end{bmatrix} \begin{bmatrix} T_{xx} \\ T_{yx} \end{bmatrix} = \begin{bmatrix} E_x^{\text{in}*} \\ E_x^{\text{out}} \end{bmatrix}, \tag{2}$$

where $*$ denotes complex conjugation. Equation 2 is important as it shows how one can find the Jones matrix required to transform any input field with a given phase and polarization, to any desired output field with a different phase and polarization. This is the first application of the birefringent meta-atoms, i.e., *complete and independent polarization and phase control*.

The Jones matrix is uniquely determined by Equation 2, unless the determinant of the coefficients matrix on the left hand side is zero. In this case, the matrix rows (i.e., $\mathbf{E}^{\text{out}*}$ and $\mathbf{E}^{\text{in}}$) will be proportional. Since the Jones matrix is unitary (i.e., the input and output powers are equal), the proportionality coefficient must have unit amplitude: $\mathbf{E}^{\text{out}*} = \exp(\text{i}\phi)\mathbf{E}^{\text{in}}$ which means that $\mathbf{E}^{\text{out}}$ and $\mathbf{E}^{\text{in}}$ have the same polarization ellipse, but an opposite handedness. The condition $\mathbf{E}^{\text{out}*} = \exp(\text{i}\phi)\mathbf{E}^{\text{in}}$ does not uniquely determine the Jones matrix. To uniquely determine the Jones matrix, two conditions for two different sets of input/output fields are necessary and can be chosen as: $\mathbf{E}_1^{\text{out}*} = \exp(\text{i}\phi_1)\mathbf{E}_1^{\text{in}}$ and $\mathbf{E}_2^{\text{out}*} = \exp(\text{i}\phi_2)\mathbf{E}_2^{\text{in}}$. Here we are using the numeral subscripts to distinguish between the two input/output field sets. If ϕ_1 and ϕ_2 can be independently controlled, then $\mathbf{E}_1^{\text{in}}$ and $\mathbf{E}_2^{\text{in}}$ (as well as $\mathbf{E}_1^{\text{out}}$ and $\mathbf{E}_2^{\text{out}}$) should be orthogonal to each other from an energy conservation argument. We can write the final equation as:

$$\begin{bmatrix} E_{1,x}^{\text{in}} & E_{1,y}^{\text{in}} \\ E_{2,x}^{\text{in}} & E_{2,y}^{\text{in}} \end{bmatrix} \begin{bmatrix} T_{xx} \\ T_{yx} \end{bmatrix} = \begin{bmatrix} E_{1,x}^{\text{out}} \\ E_{2,x}^{\text{out}} \end{bmatrix} = \begin{bmatrix} \exp(\text{i}\phi_1)E_{1,x}^{\text{in}*} \\ \exp(\text{i}\phi_2)E_{2,x}^{\text{in}*} \end{bmatrix}. \tag{3}$$

These equations are the basis for the second important application of the method: given *any* two orthogonal input polarizations (denoted by $\mathbf{E}_1^{\text{in}}$ and $\mathbf{E}_2^{\text{in}}$), their phase can be independently controlled using the Jones matrix given by Equation 3. For instance, Arbabi et. al.,[46] demonstrated a metasurface that focuses RHCP input light to a tight spot, and LHCP input light to a doughnut shape. The cost is that the output orthogonal polarizations have the opposite handedness compared

to the input ones. Once the Jones matrix is calculated from Equation 3 (or Equation 2, depending on the desired type of transformation), the two phases, $\phi_{x'}$ and $\phi_{y'}$, and the rotation angle θ can be calculated from Equation 1. Let us emphasize here that since this is a point-by-point design, all the steps can be repeated independently for each nano-post, meaning that the polarization basis can be changed from one nano-post to the next.

Based on the concept and technique just described, the first design step is identifying the input polarizations at each point. For the DoFP-PC, three different sets of H/V, $\pm 45^{\circ}$, and RHCP/LHCP are chosen, corresponding to the three distinct areas in the superpixel shown in **Figure 1**b. Then, the required phase profiles are determined to split each two orthogonal polarizations and focus them to the centers of adjacent pixels on the image sensor as shown schematically in **Figure 1**c. For a pixel size of 4.8 μm, the calculated phase profiles are shown in **Figure 2**d, where the focal distance is assumed to be 9.6 μm. Since each polarization basis covers two image sensor pixels, the phases are defined over the area of two pixels. In addition, the calculated phases are the same for the three different polarization bases, and therefore only one basis is shown in **Figure 2**d. Using these phases and knowing the desired polarization basis at each point, we calculated the rotation angles and nano-post dimensions from Equations 3 and 1 along with the data shown in **Figure 2**b.

The metasurface mask was then fabricated in a process similar to Ref.[62] A 650-nm-thick layer of α-Si was deposited on a fused silica wafer. The metasurface pattern was defined using electron-beam lithography, and transferred to the α-Si layer through a lift-off process used to form a hard etch-mask, followed by dry etching. **Figure 2**e shows a scanning electron micrograph of a fabricated superpixel, with the polarization bases denoted by arrows for each section. In addition to the metasurface mask corresponding to a pixel size of 4.8 μm that is mentioned above and shown in **Figure 2**e, two other masks with pixel sizes of 7.2 μm and 2.4 μm were also fabricated with focal distances of 14.4 μm and 4.8 μm, respectively. We used these to study the effect of pixel size on performance.

To characterize the metasurface mask we illuminated it with light from an 850-nm LED filtered by a 10-nm bandpass filter with different states of polarization. We then imaged the plane

corresponding to the image sensor location using a custom-built microscope (see Supporting Information Fig. S2 for measurement details and the setup). **Figure 3** summarizes the superpixel characterization results for the 4.8-μm pixel design. The measured Stokes parameters are plotted in **Figure 3**a for different input polarizations, showing a $<10\%$ cross-talk between polarizations and high similarity between different superpixels. The measurements were averaged over the field of view of the microscope that corresponds to about 120 superpixels. The standard deviations are shown in the graph as error bars. In addition, the intensity distribution over a sample superpixel area is shown in **Figure 3**b. The graphs show the clear ability of the metasurface mask to route light as desired for various input polarizations. Similar characterization results without a bandpass filter, corresponding to a bandwidth of about 5%, are presented in Supporting Information Figure S3. Slight performance degradation is observed with a maximum cross-talk of $\sim 13\%$ since the metasurface efficiency decreases with changing the wavelength. In addition, similar measurement results for metasurface masks with pixel sizes of 7.2 μm and 2.4 μm are presented in Supporting Information Figures S4 and S5, respectively. The results show a degradation of performance with reducing the pixel size as the cross-talk is smaller than 7.5% and 13% for 7.2-μm and 2.4-μm pixels, respectively. To show the ability of the metasurface mask to characterize the polarization state of unpolarized light, we repeated the same measurements with the polarization filter removed from the setup. **Figure 3**c summarizes the results of this measurement that determines the polarization state of light emitted by the LED. The data given in **Figure 3**a is used to estimate the calibration matrix. As expected, the emitted light has a low degree of polarization (<0.08). We also characterized the polarization state of the emitted LED light using a QWP and a linear polarizer, and found the degree of polarization to be equal to zero up to the measurement error.

In addition, we measured the transmission efficiency of the metasurface mask and found it to be in the range of 60% to 65% for all pixel size designs and input polarizations. The lower than expected transmission is mainly due to a few factors. First, the metasurface has a maximum deflection angle larger than 50°, which results in lower transmission efficiency.[37,63] Second, the relatively large metasurface lattice constant of 480 nm does not satisfy the Nyquist sampling the-

orem for the large-deflection-angle transmission masks inside the fused silica substrate.[64] This results in spurious diffraction of light inside the substrate. Finally, the mask is periodic with a larger-than-wavelength period equal to the superpixel dimensions. This results in excitation of the higher diffraction orders especially inside the substrate that has a higher refractive index. It is worth noting that the achieved $\sim$65% efficiency is higher than the 50% theoretical limit of a polarimetric camera that is based on polarization filtering.

Finally, we show polarimetric imaging using the DoFP metasurface mask. We designed and used a custom dielectric metasurface polarization mask as the imaging target. We utilized the polarization-phase control method described above, and a fabrication process similar to the DoFP metasurface mask for the imaging target. The mask converts x-polarized input light to an output polarization state characterized by the polarization ellipses and the Stokes parameters shown in **Figure 4**a and **Figure 4**b, respectively. Each Stokes parameter is +1 or -1 in an area of the image corresponding to the specific polarization. For instance, S_3 is +1 in the right half circle, -1 in the left half circle, and 0 elsewhere. Using a second custom-built microscope, the image of the polarization mask was projected on the DoFP metasurface mask (see Supporting Information Figure S2 for the measurement setup and the details). First, we removed the metasurface mask and performed a conventional polarimetric imaging of the projected image using a linear polarizer and a QWP. To this end, six different images were captured with different rotations of the linear polarizer and the QWP to determine the Stokes parameters. The results are shown in **Figure 4**c. Second, we removed the linear polarizer and the QWP and inserted the DoFP metasurface mask. The Stokes parameters were extracted from a single image captured at the focal plane of the DoFP metasurface mask. The results are shown in **Figure 4**d, and are in good agreement with the results of regular polarimetric imaging. The lower quality of the metasurface polarimetric camera image is mainly due to the limited number of superpixels that fit inside the single field of view of the microscope. The field of view is limited by the microscope magnification and image sensor size which are $\times$22 and $\sim$15 mm, respectively. This results in a low resolution of 70-by-46 points for the metasurface polarimetric image versus the $\sim$2000-by-2000 point resolution of the regular

polarimetric image. In addition, to form the final image, we need to know the coordinates of each superpixel a priori. The existing errors in estimating these coordinates that result from small tilts in the setup, aberrations of the custom-built microscope, and etc. cause a degraded performance over some superpixels. In a polarization camera made using the DoFP metasurface mask, both of these issues will be resolved as the resolution can be much higher, and the mask and image sensor are lithographically aligned.

To extract the polarization information of the image we integrated the intensity inside the area of two adjacent image sensor pixels. Then, we calculated the corresponding Stokes parameter simply by dividing the difference between the two measured intensities by their sum. While straightforward, this is not the optimal method to perform this task as there is non-negligible cross-talk between different polarization intensities measured by the pixels (**Figure 3**). The issue becomes more pronounced moving toward smaller pixel sizes as seen for the 2.4-μm case (Supporting Information Figure S5). To address this issue, a better polarization extraction method is to form a calibration matrix that relates the actual intensities to the corresponding measured values for a specific DoFP metasurface mask design (for instance using the data in **Figure 3**). This allows one to reduce the effect of the cross-talk and measure the polarization state more precisely.

The designed small focal distances (e.g., 9.6 μm for the 4.8-μm pixel) result in an upper limit of 40% for the operation bandwidth of the device due to diffractive chromatic dispersion. To get this upper limit we assumed a constant phase profile that doesn't change with wavelength and used the criterion given in.[47] Therefore, the actual bandwidth of the device is limited by the focusing and polarization control efficiencies that drop with detuning from the design wavelength. In addition, it is expected that the same level of performance achieved from the 2.4-μm pixel in this work, can be achieved from a $\sim$1.7-μm pixel if the material between the mask and the image sensor has a refractive index of 1.5, which is the case when the DoFP mask is separated from the image sensor by an oxide or polymer layer as would be the case in a realistic device. To achieve smaller pixel sizes, better performance, and larger operation bandwidths one could use more advanced optimization[65] or chromatic-dispersion control techniques,[66] especially since the size of a single

superpixel is small and allows for a fast simulation of the forward problem. In addition, a spatial multiplexing scheme[67–70] can be used to interleave multiple superpixels corresponding to different optical bands, and therefore make a color-polarization camera.

Using the polarization-phase control method and the platform introduced in,[46] we demonstrated a metasurface mask for DoFP-PCs. The mask is designed to split and focus light to six different pixels on an image sensor for three different polarization bases. This allows for complete characterization of polarization by measuring the four Stokes parameters over the area of each superpixel which corresponds to the area of six pixels on an image sensor. We experimentally demonstrated the ability of the metasurface masks to correctly measure the polarization state for different input polarizations. In addition, we used the DoFP metasurface mask to form an image of a complicated polarization object, showing the ability to make a polarization camera. Many of the limitations faced here can be overcome using more advanced optimization techniques or better data extraction methods. We anticipate that polarization cameras based on metasurface masks will be able to replace the conventional polarization cameras for many applications as they enable measurement of the full polarization state including the degree of circular polarization and handedness.

Methods

Simulation and design. To design the DoFP metasurface mask, we first calculated the two phase profiles required for the two polarization states [**Figure 2**d]. The phase profiles correspond to decentered aspheric lenses that focus each polarization at the center of one image sensor pixel. These phases are then used in Equation 3 along with the known input polarization states to calculate the Jones matrix. To find the nano-post corresponding to each Jones matrix, the matrix is diagonalized according to Equation 1, and the two phases, $\phi_{x'}$ and $\phi_{y'}$, and the rotation angle θ are then extracted. The dimensions of the nano-post providing the required pair of phases is then found using the data in **Figure 2**b.

The polarization target used for the imaging experiments in **Figure 4** was designed in a slightly different manner since in this case only the output polarization is of interest. Assuming an x-polarized input light, the output polarization at each point on the mask was chosen according to **Figure 4**a. In the general case, the mask can then be designed using the Jones matrix found from Equation 2. In this special case, however, the device is a set of nano-posts acting as quarter or half wave-plates. Therefore, we designed the nano-posts in a manner similar to[71] to make it robust to fabrication errors.

To find the transmission amplitude and phase for the nano-posts [Supporting Information Figure S1] we simulated a uniform array of nano-posts with rectangular cross-sections under normally incident x- and y-polarized light using the rigorous coupled wave analysis.[61] The resulting complex transmissions were then used to find the best nano-post that provides each required phase pair through minimizing the Euclidean distance between $[e^{i\phi_x}, e^{i\phi_y}]$ and $[t_x, t_y]$, where ϕ_x and ϕ_y are the desired phase values, and t_x and t_y are complex nano-post transmissions. The optimized nano-post dimensions are plotted in **Figure 2**b.

Fabrication. The fabrication process is the same for both the DoFP metasurface mask and the polarization imaging target. The fabrication started with deposition of a 650-nm-thick layer of α-Si on a 500-μm-thick fused silica substrate. The metasurface pattern is defined in a $\sim$300-nm-thick ZEP-520A positive electron-beam resist using electron-beam lithography. After development of the resist, a $\sim$70-nm-thick layer of aluminum oxide is deposited on the sample using electron-beam evaporation and lifted off to invert the pattern. The aluminum oxide is then used as a hard mask in the reactive ion etching of the α-Si layer. Finally, the aluminum oxide mask is removed in a solution of hydrogen peroxide and ammonium hydroxide.

Measurement. The measurement setups (including part models) are schematically illustrated in Supporting Information Figure S2 for different parts of the characterization process. To characterize the DoFP super-pixel performance, light from an LED was passed through a linear polarizer and a QWP to set the input polarization state. The six different polarization states [**Figure 3**a] were generated using this combination. The intensity distribution patterns at the focal plane after

the DoFP metasurface mask were then imaged using a custom-built microscope. The data was analyzed by calculating the Stokes parameters measured by each super-pixel, and averaging over all the super-pixels that fit within the field of view. A 10-nm bandwidth filter with a center wavelength of 850 nm was inserted in the path to characterize the narrow-band operation, and was then removed to acquire the results for a wider-bandwidth source.

The imaging polarimetry experiments were performed in a similar way. For these experiments, the polarization target was illuminated by *x*-polarized light out of a supercontinuum laser source (filtered by the same 10-nm bandwidth filter). The target was imaged onto the DoFP metasurface mask plane using a secondary custom-built microscope (operating as relay optics). The intensity distribution at the focal plane after the DoFP metasurface mask was then imaged and analyzed to generate the polarization images plotted in **Figure 4**d. For comparison, the DoFP metasurface mask was removed and a polarization analyzer (i.e., a QWP and a linear polarizer) was inserted into the system to form the reference polarization images plotted in **Figure 4**c.

Acknowledgements. This work was supported by the DARPA EXTREME program. We gratefully acknowledge critical support and infrastructure provided for this work by the Kavli Nanoscience Institute at Caltech.

Author Contributions. E.A., A.A., and A.F. conceived of the experiments. E.A., S.M.K., and A.A. designed and fabricated the devices. E.A. and S.M.K. performed the measurements and analyzed the data. E.A. and A.F. wrote the manuscript. All authors discussed the results and the manuscript.

Notes. The authors declare no competing financial interests.

Supporting Information. Extended simulation data for the metasurface platform. Measurement setup details. Measurement results of the metasurface masks with other pixel sizes.

References

(1) Chang, C.-I. *Hyperspectral imaging: techniques for spectral detection and classification*; Springer Science & Business Media, 2003; Vol. 1.

(2) Sun, D.-W. *Hyperspectral imaging for food quality analysis and control*; Elsevier, 2010.

(3) Tyo, J. S.; Goldstein, D. L.; Chenault, D. B.; Shaw, J. A. Review of passive imaging polarimetry for remote sensing applications. *Appl. Opt.* **2006**, *45*, 5453–5469.

(4) Garcia, N. M.; de Erausquin, I.; Edmiston, C.; Gruev, V. Surface normal reconstruction using circularly polarized light. *Opt. Express* **2015**, *23*, 14391–14406.

(5) Coffeen, D. L. Polarization and scattering characteristics in the atmospheres of Earth, Venus, and Jupiter. *J. Opt. Soc. Am.* **1979**, *69*, 1051–1064.

(6) Walraven, R. Polarization Imagery. SPIE Opt. Eng. 1981; p 200114.

(7) Egan, W. G.; Johnson, W. R.; Whitehead, V. S. Terrestrial polarization imagery obtained from the Space Shuttle:characterization and interpretation. *Appl. Opt.* **1991**, *30*, 435–442.

(8) Liu, Y.; York, T.; Akers, W.; Sudlow, G.; Gruev, V.; Achilefu, S. Complementary fluorescence-polarization microscopy using division-of-focal-plane polarization imaging sensor. *J. Biomed. Opt.* **2012**, *17*, 116001.

(9) Roberts, N. W.; How, M. J.; Porter, M. L.; Temple, S. E.; Caldwell, R. L.; Powell, S. B.; Gruev, V.; Marshall, N. J.; Cronin, T. W. Animal Polarization Imaging and Implications for Optical Processing. *Proceed. IEEE* **2014**, *102*, 1427–1434.

(10) Charanya, T.; York, T.; Bloch, S.; Sudlow, G.; Liang, K.; Garcia, M.; Akers, W. J.; Rubin, D.; Gruev, V.; Achilefu, S. Trimodal color-fluorescence-polarization endoscopy aided by a tumor selective molecular probe accurately detects flat lesions in colitis-associated cancer. *J. Biomed. Opt.* **2014**, *19*, 14.

(11) Garcia, M.; Edmiston, C.; Marinov, R.; Vail, A.; Gruev, V. Bio-inspired color-polarization imager for real-time in situ imaging. *Optica* **2017**, *4*, 1263–1271.

(12) Johnson, J. Infrared polarization signature feasibility tests. *US Army Mobility Equipment Research and Development Center* **1974**, *TR-EO-74-1 (AD COO1-133)*.

(13) Chin-Bing, S. Infrared polarization signature analysis. *Defense Technical Information Center* **1976**, *Rep. ADC008418*.

(14) Solomon, J. E. Polarization imaging. *Appl. Opt.* **1981**, *20*, 1537–1544.

(15) Pezzaniti, J. L.; Chipman, R. A. Mueller matrix imaging polarimetry. Opt. Eng. 1995; p 11.

(16) Nordin, G. P.; Meier, J. T.; Deguzman, P. C.; Jones, M. W. Micropolarizer array for infrared imaging polarimetry. *J. Opt. Soc. Am. A* **1999**, *16*, 1168–1174.

(17) Guo, J.; Brady, D. Fabrication of thin-film micropolarizer arrays for visible imaging polarimetry. *Appl. Opt.* **2000**, *39*, 1486–1492.

(18) Gruev, V.; Spiegel, J. V. d.; Engheta, N. Image sensor with focal plane extraction of polarimetric information. 2006 IEEE International Symposium on Circuits and Systems. 2006; pp 4 pp.–216.

(19) Rust, D. Integrated dual imaging detector. USPatent **1995**, 5,438,414.

(20) Andreou, A. G.; Kalayjian, Z. K. Polarization imaging: principles and integrated polarimeters. *IEEE Sens. Jour.* **2002**, *2*, 566–576.

(21) Gruev, V.; Ortu, A.; Lazarus, N.; Spiegel, J. V. d.; Engheta, N. Fabrication of a dual-tier thin film micropolarization array. *Opt. Exp.* **2007**, *15*, 4994–5007.

(22) Gruev, V.; Perkins, R.; York, T. CCD polarization imaging sensor with aluminum nanowire optical filters. *Opt. Express* **2010**, *18*, 19087–19094.

(23) Deguzman, P. C.; Nordin, G. P. Stacked subwavelength gratings as circular polarization filters. *Appl. Opt.* **2001**, *40*, 5731–5737.

(24) Myhre, G.; Hsu, W.-L.; Peinado, A.; LaCasse, C.; Brock, N.; Chipman, R. A.; Pau, S. Liquid crystal polymer full-stokes division of focal plane polarimeter. *Opt. Express* **2012**, *20*, 27393–27409.

(25) Hsu, W.-L.; Myhre, G.; Balakrishnan, K.; Brock, N.; Ibn-Elhaj, M.; Pau, S. Full-Stokes imaging polarimeter using an array of elliptical polarizer. *Opt. Express* **2014**, *22*, 3063–3074.

(26) Hsu, W.-L.; Davis, J.; Balakrishnan, K.; Ibn-Elhaj, M.; Kroto, S.; Brock, N.; Pau, S. Polarization microscope using a near infrared full-Stokes imaging polarimeter. *Opt. Express* **2015**, *23*, 4357–4368.

(27) Kamali, S. M.; Arbabi, E.; Arbabi, A.; Faraon, A. A review of dielectric optical metasurfaces for wavefront control. *Nanophotonics* **2018**, *7*, 1041–1068.

(28) Kuznetsov, A. I.; Miroshnichenko, A. E.; Brongersma, M. L.; Kivshar, Y. S.; Lukyanchuk, B. Optically resonant dielectric nanostructures. *Science* **2016**, *354*.

(29) Staude, I.; Schilling, J. Metamaterial-inspired silicon nanophotonics. *Nat. Photon.* **2017**, *11*, 274–284.

(30) Hsiao, H.-H.; Chu, C. H.; Tsai, D. P. Fundamentals and Applications of Metasurfaces. *Small Methods* **2017**, *1*, 1600064.

(31) Astilean, S.; Lalanne, P.; Chavel, P.; Cambril, E.; Launois, H. High-efficiency subwavelength diffractive element patterned in a high-refractive-index material for 633 nm. *Opt. Lett.* **1998**, *23*, 552–554.

(32) Lalanne, P.; Astilean, S.; Chavel, P.; Cambril, E.; Launois, H. Blazed binary subwavelength gratings with efficiencies larger than those of conventional échelette gratings. *Opt. Lett.* **1998**, *23*, 1081–1083.

(33) Fattal, D.; Li, J.; Peng, Z.; Fiorentino, M.; Beausoleil, R. G. Flat dielectric grating reflectors with focusing abilities. *Nat. Photon.* **2010**, *4*, 466–470.

(34) Lu, F.; Sedgwick, F. G.; Karagodsky, V.; Chase, C.; Chang-Hasnain, C. J. Planar high-numerical-aperture low-loss focusing reflectors and lenses using subwavelength high contrast gratings. *Opt. Express* **2010**, *18*, 12606–12614.

(35) Vo, S.; Fattal, D.; Sorin, W. V.; Zhen, P.; Tho, T.; Fiorentino, M.; Beausoleil, R. G. Sub-Wavelength Grating Lenses With a Twist. *IEEE Photon. Technol. Lett.* **2014**, *26*, 1375–1378.

(36) Lin, D.; Fan, P.; Hasman, E.; Brongersma, M. L. Dielectric gradient metasurface optical elements. *Science* **2014**, *345*, 298–302.

(37) Arbabi, A.; Horie, Y.; Ball, A. J.; Bagheri, M.; Faraon, A. Subwavelength-thick lenses with high numerical apertures and large efficiency based on high-contrast transmitarrays. *Nat. Commun.* **2015**, *6*, 7069.

(38) Khorasaninejad, M.; Chen, W. T.; Devlin, R. C.; Oh, J.; Zhu, A. Y.; Capasso, F. Metalenses at visible wavelengths: Diffraction-limited focusing and subwavelength resolution imaging. *Science* **2016**, *352*, 1190–1194.

(39) Yin, X.; Steinle, T.; Huang, L.; Taubner, T.; Wuttig, M.; Zentgraf, T.; Giessen, H. Beam switching and bifocal zoom lensing using active plasmonic metasurfaces. *Light: Sci. Appl.* **2017**, *6*, e17016.

(40) Schlickriede, C.; Waterman, N.; Reineke, B.; Georgi, P.; Li, G.; Zhang, S.; Zentgraf, T. Imaging through Nonlinear Metalens Using Second Harmonic Generation. *Adv. Mater.* **2018**, *30*, 1703843.

(41) Komar, A.; Fang, Z.; Bohn, J.; Sautter, J.; Decker, M.; Miroshnichenko, A.; Pertsch, T.; Brener, I.; Kivshar, Y. S.; Staude, I. e. a. Electrically tunable all-dielectric optical metasurfaces based on liquid crystals. *Appl. Phys. Lett.* **2017**, *110*, 071109.

(42) Paniagua-Dominguez, R.; Yu, Y.; Khaidarov, E.; Choi, S.; Leong, V.; Bakker, R. M.; Liang, X.; Fu, Y. H.; Valuckas, V.; Krivitsky, L. A. e. a. A metalens with near-unity numerical aperture. *Nano Lett.* **2018**, *18*, 2124–2132.

(43) Zhan, A.; Colburn, S.; Dodson, C. M.; Majumdar, A. Metasurface Freeform Nanophotonics. *Sci. Rep.* **2017**, *7*, 1673.

(44) Thyagarajan, K.; Sokhoyan, R.; Zornberg, L.; Atwater, H. A. Millivolt Modulation of Plasmonic Metasurface Optical Response via Ionic Conductance. *Adv. Mater.* **2017**, *29*, 1701044.

(45) Kamali, S. M.; Arbabi, E.; Arbabi, A.; Horie, Y.; Faraji-Dana, M.; Faraon, A. Angle-Multiplexed Metasurfaces: Encoding Independent Wavefronts in a Single Metasurface under Different Illumination Angles. *Phys. Rev. X* **2017**, *7*, 041056.

(46) Arbabi, A.; Horie, Y.; Bagheri, M.; Faraon, A. Dielectric metasurfaces for complete control of phase and polarization with subwavelength spatial resolution and high transmission. *Nat. Nanotechnol.* **2015**, *10*, 937–943.

(47) Arbabi, A.; Arbabi, E.; Kamali, S. M.; Horie, Y.; Han, S.; Faraon, A. Miniature optical planar camera based on a wide-angle metasurface doublet corrected for monochromatic aberrations. *Nat. Commun.* **2016**, *7*, 13682.

(48) Arbabi, A.; Arbabi, E.; Horie, Y.; Kamali, S. M.; Faraon, A. Planar metasurface retroreflector. *Nat. Photon.* **2017**, *11*, 415–420.

(49) Groever, B.; Chen, W. T.; Capasso, F. Meta-Lens Doublet in the Visible Region. *Nano Lett.* **2017**, *17*, 4902–4907.

(50) Arbabi, E.; Arbabi, A.; Kamali, S. M.; Horie, Y.; Faraji-Dana, M.; Faraon, A. MEMS-tunable dielectric metasurface lens. *Nat. Commun.* **2018**, *9*, 812.

(51) Ellenbogen, T.; Seo, K.; Crozier, K. B. Chromatic Plasmonic Polarizers for Active Visible Color Filtering and Polarimetry. *Nano Lett.* **2012**, *12*, 1026–1031.

(52) Wen, D.; Yue, F.; Kumar, S.; Ma, Y.; Chen, M.; Ren, X.; Kremer, P. E.; Gerardot, B. D.; Taghizadeh, M. R.; Buller, G. S. e. a. Metasurface for characterization of the polarization state of light. *Opt. Express* **2015**, *23*, 10272–10281.

(53) Khorasaninejad, M.; Zhu, W.; Crozier, K. B. Efficient polarization beam splitter pixels based on a dielectric metasurface. *Optica* **2015**, *2*, 376–382.

(54) Pors, A.; Nielsen, M. G.; Bozhevolnyi, S. I. Plasmonic metagratings for simultaneous determination of Stokes parameters. *Optica* **2015**, *2*, 716–723.

(55) Chen, W. T.; Torok, P.; Foreman, M. R.; Liao, C. Y.; Tsai, W. Y.; Wu, P. R.; Tsai, D. P. Integrated plasmonic metasurfaces for spectropolarimetry. *Nanotechnology* **2016**, *27*, 224002.

(56) Balthasar Mueller, J. P.; Leosson, K.; Capasso, F. Ultracompact metasurface in-line polarimeter. *Optica* **2016**, *3*, 42–47.

(57) Ding, F.; Pors, A.; Chen, Y.; Zenin, V. A.; Bozhevolnyi, S. I. Beam-Size-Invariant Spectropolarimeters Using Gap-Plasmon Metasurfaces. *ACS Photonics* **2017**, *4*, 943–949.

(58) Maguid, E.; Yulevich, I.; Yannai, M.; Kleiner, V.; Brongersma, M. L.; Hasman, E. Multifunctional interleaved geometric-phase dielectric metasurfaces. *Light: Sci. Appl.* **2017**, *6*, e17027.

(59) Wei, S.; Yang, Z.; Zhao, M. Design of ultracompact polarimeters based on dielectric metasurfaces. *Opt. Lett.* **2017**, *42*, 1580–1583.

(60) Huard, S. *Polarization of light*; Wiley-VCH, 1997; Vol. 1.

(61) Liu, V.; Fan, S. S4 : A free electromagnetic solver for layered periodic structures. *Comput. Phys. Commun.* **2012**, *183*, 2233–2244.

(62) Arbabi, E.; Arbabi, A.; Kamali, S. M.; Horie, Y.; Faraon, A. High efficiency double-wavelength dielectric metasurface lenses with dichroic birefringent meta-atoms. *Opt. Express* **2016**, *24*, 18468–18477.

(63) Arbabi, A.; Arbabi, E.; Kamali, S. M.; Horie, Y.; Han, S.; Faraon, A. Increasing efficiency of high-NA metasurface lenses. SPIE Photon. West. 2017; pp 101130K–1.

(64) Kamali, S. M.; Arbabi, E.; Arbabi, A.; Horie, Y.; Faraon, A. Highly tunable elastic dielectric metasurface lenses. *Laser Photon. Rev.* **2016**, *10*, 1062–1062.

(65) Sell, D.; Yang, J.; Doshay, S.; Yang, R.; Fan, J. A. Large-Angle, Multifunctional Metagratings Based on Freeform Multimode Geometries. *Nano Lett.* **2017**, *17*, 3752–3757.

(66) Arbabi, E.; Arbabi, A.; Kamali, S. M.; Horie, Y.; Faraon, A. Controlling the sign of chromatic dispersion in diffractive optics with dielectric metasurfaces. *Optica* **2017**, *4*, 625–632.

(67) Bayer, B. Color imaging array. US Patent **1976**, 3,971,065.

(68) Arbabi, E.; Arbabi, A.; Kamali, S. M.; Horie, Y.; Faraon, A. Multiwavelength metasurfaces through spatial multiplexing. *Sci. Rep.* **2016**, *6*, 32803.

(69) Lin, D.; Holsteen, A. L.; Maguid, E.; Wetzstein, G.; Kik, P. G.; Hasman, E.; Brongersma, M. L. Photonic Multitasking Interleaved Si Nanoantenna Phased Array. *Nano Lett.* **2016**, *16*, 7671–7676.

(70) Hu, J.; Liu, C.-H.; Ren, X.; Lauhon, L. J.; Odom, T. W. Plasmonic Lattice Lenses for Multi-wavelength Achromatic Focusing. *ACS Nano* **2016**, *10*, 10275–10282.

(71) Backlund, M. P.; Arbabi, A.; Petrov, P. N.; Arbabi, E.; Saurabh, S.; Faraon, A.; Moerner, W. E. Removing orientation-induced localization biases in single-molecule microscopy using a broadband metasurface mask. *Nat. Photon.* **2016**, *10*, 459–462.

Figures

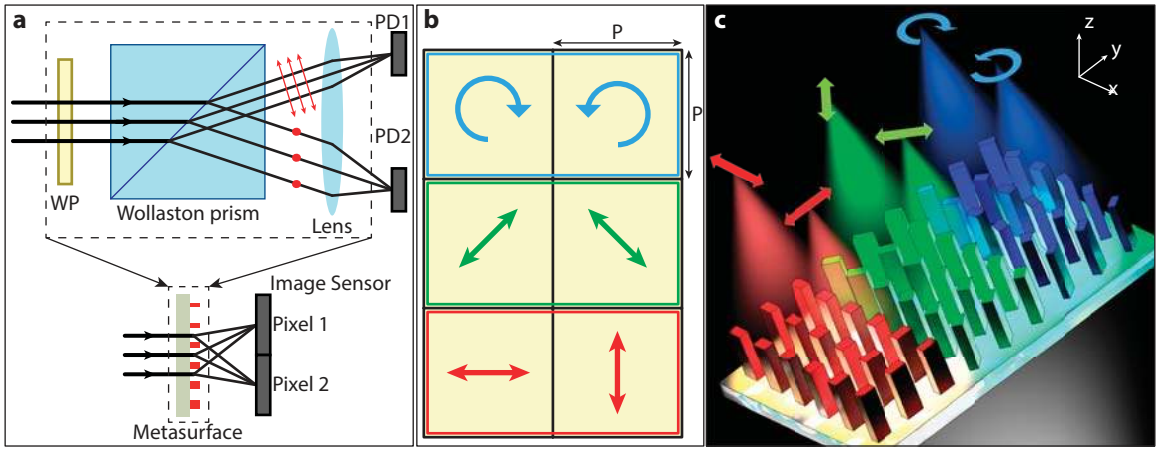

Figure 1 . Concept of a metasurface polarization camera. **(a)** Top: Schematics of a conventional setup used for polarimetry: a waveplate (quarter or half) followed by a Wollaston prism and a lens that focuses light on detectors. Bottom: A compact metasurface implements the functionality of all three components combined, and can be directly integrated on an image sensor. WP: waveplate; PD: photodetector. **(b)** A possible arrangement for a superpixel of the polarization camera, comprising six image sensor pixels. Three independent polarization basis (H/V, $\pm 45°$, and RHCP/LHCP) are chosen to measure the Stokes parameters at each superpixel. **(c)** Three-dimensional illustration of a superpixel focusing different polarizations to different spots. The colors are used only for clarity of the image and bear no wavelength information.

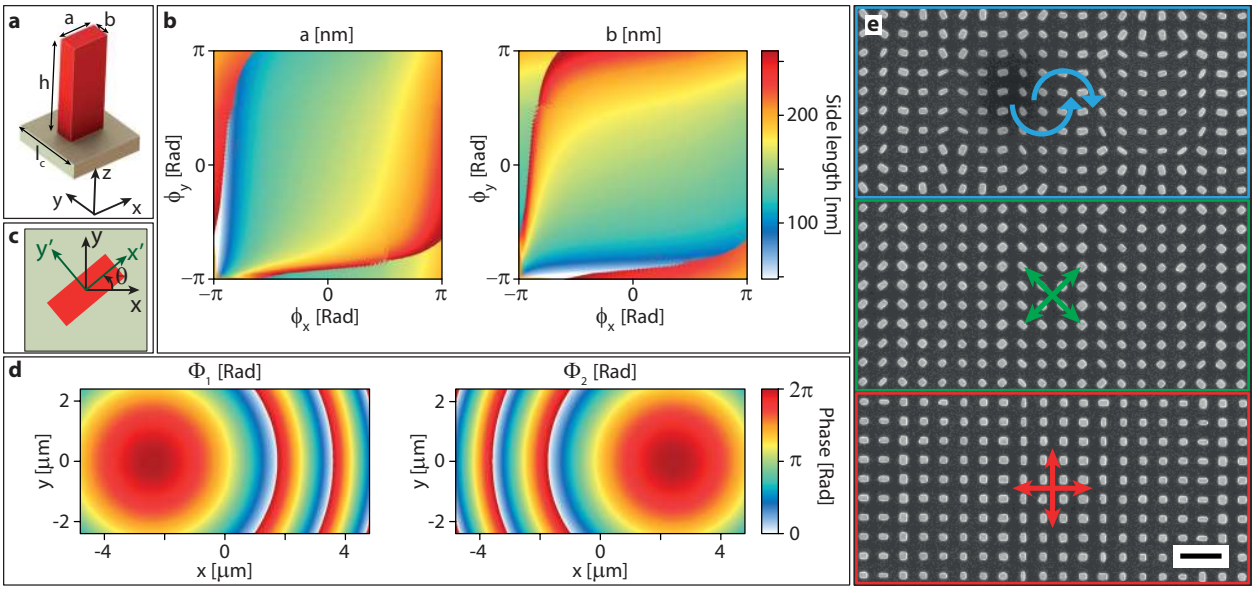

Figure 2 . Meta-atom and pixel design. **(a)** An α-Si nano-post with a rectangular cross section resting on a glass substrate provides full polarization and phase control. **(b)** Design graphs used for finding the in-plane dimensions of a nano-post. Given a pair of transmission phases ϕ_x and ϕ_y, one can find the corresponding nano-post dimensions a and b from the two graphs. The nano-posts are 650 nm tall, and the lattice constant is 480 nm. **(c)** Schematic illustration of a rotated nano-post, showing the rotation angle and the old and the new optical axis sets. **(d)** Required phase profiles for a metasurface that does both polarization beam splitting and focusing at two orthogonal polarizations. These can be any set of orthogonal polarizations, linear or elliptical. The focal distance for these phase profiles is 9.6 μm, equal to the width of the superpixel in the x direction. The lateral positions of the focal spots are x= $\pm$2.4 μm and y=0. **(e)** Scanning electron micrograph of a fabricated superpixel. The polarization basis for each part is shown with the colored arrows. Scale bar: 1 μm.

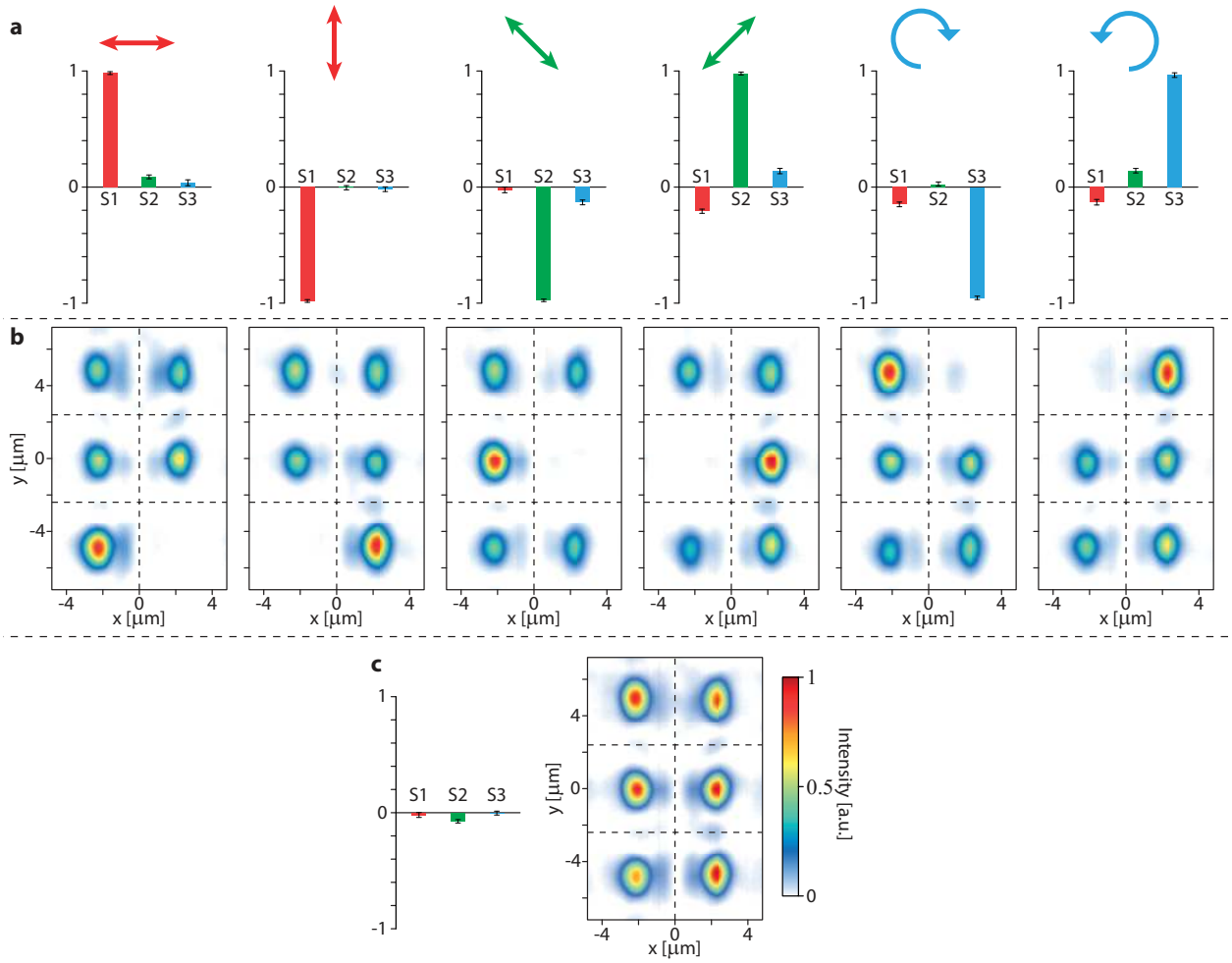

Figure 3 . Characterization results of the superpixels of the DoFP metasurface mask. **(a)** Measured average Stokes parameters for different input polarizations (shown with colored arrows), and **(b)** the corresponding intensity distributions for a sample superpixel. The Stokes parameters are averaged over about 120 superpixels (limited by the microscope field of view), and the error bars represent the statistical standard deviations. **(c)** Measured average Stokes parameters and the corresponding intensity distribution for the LED light source without any polarization filters in the setup. All the measurements are performed with an 850-nm LED filtered by a bandpass filter (center: 850 nm, FHMW: 10 nm) as the light source.

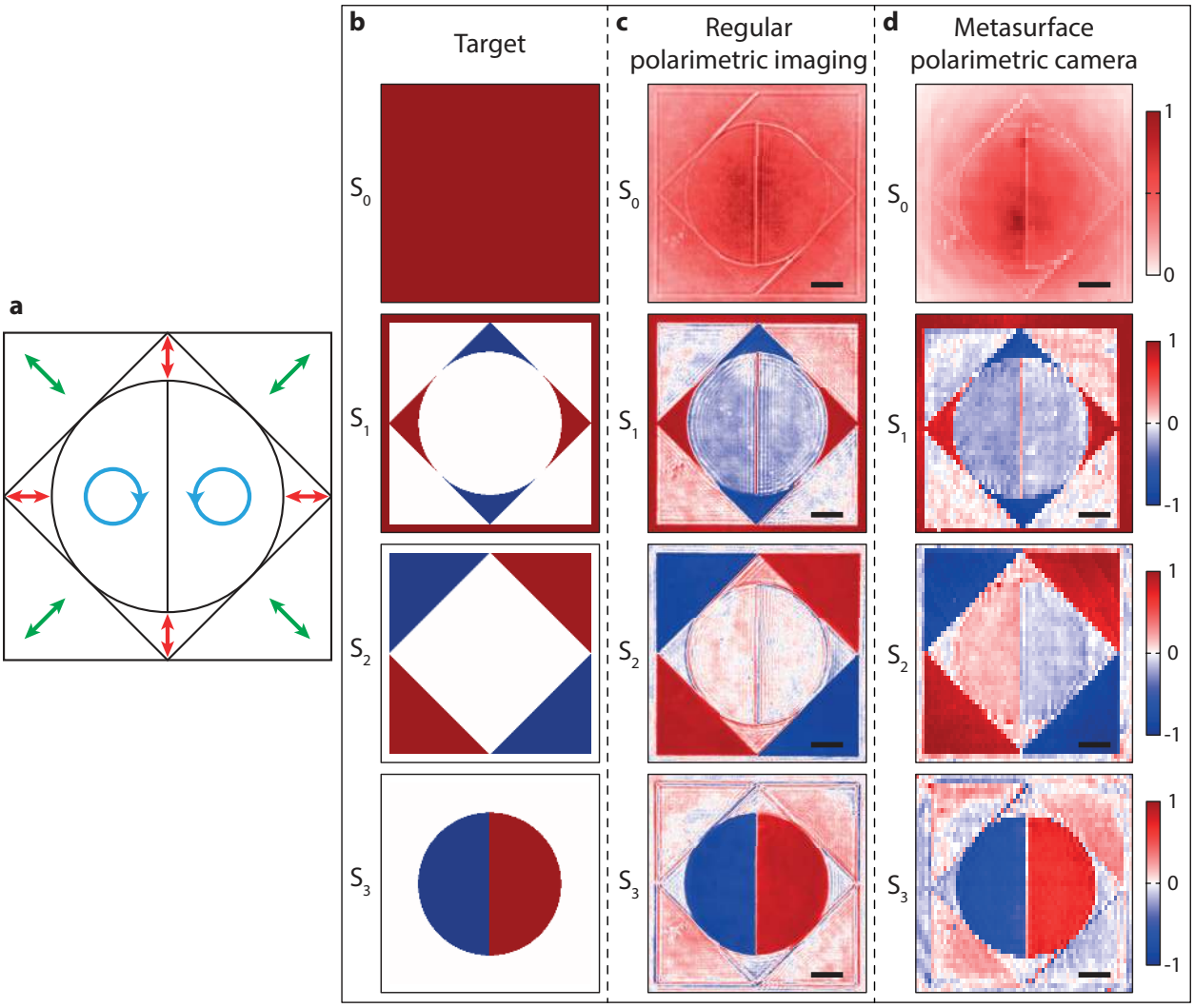

Figure 4 . Polarimetric imaging. **(a)** Schematic illustration of target polarization ellipse in different parts of the polarization sample. Stokes parameters of the polarization sample: **(b)** the targeted polarization mask, **(c)** the fabricated mask imaged using conventional polarimetry, and **(d)** the same mask imaged using the metasurface polarimetric camera. The scale bars denote 100 μm in the metasurface polarization camera mask plane.

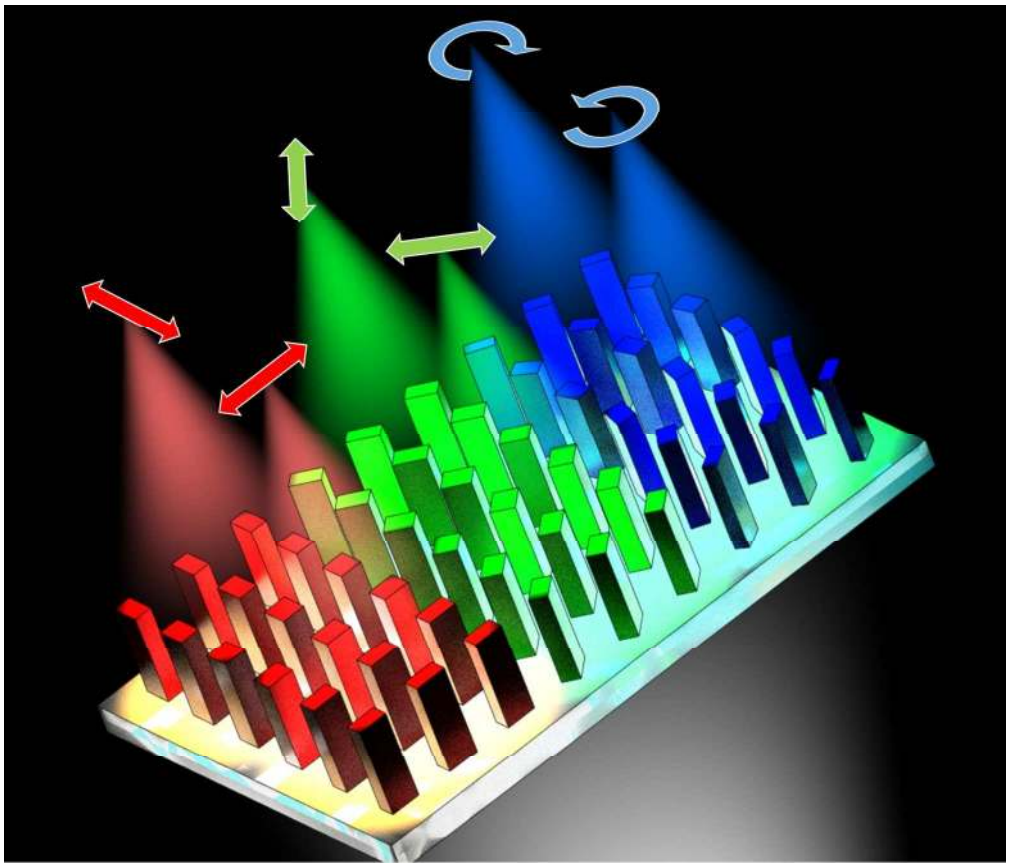

TOC Graphics

254x217mm (150 x 150 DPI)